Materials Horizons

Flexible Point-of-Use Phosphate Electrochemical Sensors Based on Electrodeposited Molybdenum Oxide

Journal:	*Materials Horizons*
Manuscript ID	MH-COM-04-2025-000692.R2
Article Type:	Communication
Date Submitted by the Author:	29-May-2025

Complete List of Authors:	Yu, Siqi; University of California San Diego, Department of Electrical and Computer Engineering Sun, Xiyu; University of California San Diego, Department of Electrical and Computer Engineering Yu, Zinan; The University of Utah, Department of Chemistry Jung, Jinwook; University of California San Diego, Program in Materials Science and Engineering Ishii, Satoshi; University of Minnesota Twin Cities Hayes, Christopher T.; University of Southern Mississippi School of Ocean Science and Engineering Pierre, Valerie; The University of Utah Flood, Amar; Indiana University, Department of Chemistry Azoulay, Jason; Georgia Institute of Technology, Chemistry Ng, Tse Nga; University of California San Diego, Department of Electrical and Computer Engineering; University of California San Diego

New concepts

Given phosphate's importance to biological systems, rapid in-situ phosphate monitoring is highly desirable across various fields, from health diagnostics to environmental sustainability. Whereas conventional spectroscopic assays have been lacking in portability, this work introduces a point-of-use electrochemical sensor with electrodeposited mixed-valence molybdenum oxide on flexible electrodes, enabling selective phosphate detection in complex aqueous environments. The molybdate-phosphate coordination complexes generate robust, stable redox signals without issues of dissolution and degradation in prior sensors. Integrated with a wireless potentiostat, the sensor is validated to accurately track phosphate levels in environmental and health-related samples, demonstrating a promising low-cost platform for portable phosphate sensing.

The data that support the findings of this study are available from the corresponding author upon reasonable request.

Flexible Point-of-Use Phosphate Electrochemical Sensors Based on Electrodeposited Molybdenum Oxide

Siqi Yu,[a] Xiyu Sun,[a] Zinan Yu,[b] Jinwook Jung,[c] Satoshi Ishii,[d] Christopher T. Hayes,[e] Valérie C. Pierre,[b] Amar Flood,[f] Jason D. Azoulay,[g] and Tse Nga Ng*[a,c]

[a] Department of Electrical and Computer Engineering, University of California San Diego, La Jolla, CA 92093, USA

[b] Department of Chemistry, The University of Utah, Salt Lake City, UT 84112, USA

[c] Program in Materials Science and Engineering, University of California San Diego, La Jolla, CA 92093, USA

[d] Department of Soil, Water, and Climate, University of Minnesota, St. Paul, MN 55108, USA

[e] School of Ocean Science and Engineering, University of Southern Mississippi, Stennis Space Center, MS 39529, USA

[f] Department of Chemistry, Indiana University, Bloomington, IN 47405, USA

[g] School of Chemistry and Biochemistry and School of Materials Science and Engineering, Center for Organic Photonics and Electronics, Georgia Institute of Technology, Atlanta, GA 30332, USA

*Email: tnn046@ucsd.edu

Abstract

To enable in-situ phosphate monitoring for healthcare and environmental sustainability, this work demonstrates an electrochemical sensor based on electrodeposited mixed-valence molybdenum oxide (MoO_x) for selective phosphate sensing in complex aqueous media. The MoO_x film induces strong, specific detection through coordination between Mo centers and phosphate anions, generating well-defined redox signals under square wave voltammetry. The sensor exhibits a broad linear dynamic range between 10–1000 µM, a sensitive detection limit of 8 µM, and high specificity against competing anions including Cl^-, SO_4^{2-}, NO_3^-, CO_3^{2-}, and SiO_3^{2-}. The sensors accurately measure phosphate levels in artificial saliva and influent wastewater field samples, with results validated to match those of standard molybdenum blue assays. The compact, flexible system achieves stable performance across varying ionic strengths, proving its robustness as a low-cost point-of-use monitoring platform for phosphate.

Introduction

Phosphate plays a vital role in the health of individuals to entire ecological systems.[1,2] Dysregulation of phosphate levels in the human body is linked to various diseases.[3–5] Excessive phosphate accumulation in the environment leads to pollution of water sources and eutrophication.[6–9] The capability to conduct in-situ monitoring of phosphate anions is critical for timely intervention to address imbalances and mitigate health and environmental impacts.

Various phosphate recognition strategies ranging from supramolecular receptors[2,10,11] to metal ion coordination assays[12–14] have been demonstrated, but they often rely on spectrophotometric methods that require ex-situ sample preparation and restrict measurement portability. For example, the standard for orthophosphate (PO_4^{3-}) detection is a colorimetric approach based on molybdate reaction in solution. Phosphate reacts with molybdate under acidic conditions to form phosphomolybdic acid, which is further reduced into phosphomolybdenum blue compounds with strong absorbance, following the equation $PO_4^{3-} + 12\ MoO_4^{2-} + 27\ H^+ \rightarrow H_3PO_4(MoO_3)_{12} + 12\ H_2O$.[15,16] The detailed reaction mechanisms are strongly influenced by the reaction pH, the concentrations and ratios of the reactants, and the order in which the reagents are introduced.This reaction combines strong metal-phosphate coordination with polyoxometalate cluster formation, offering high selectivity and minimal binding interference from other anions. However, this classic molybdate method requires multiple reagent addition steps and many fluid transfers,[16,17] making it unsuitable for portable detection.

To enable point-of-use monitoring, researchers are developing electrochemical sensors[18–27] for phosphate detection, mostly by transducing redox activities of phosphomolybdate species into electrical signals. Previously the sensor electrodes were made selective to phosphate by depositing molybdate on nanowires or polymer matrices. In contrast, this work shows that direct electrodeposition of molybdate precursors onto graphite carbon electrodes improves sensitivity while simplifying the fabrication process. The electrodes are patterned by low-cost printing[28–33] on flexible substrates that enable compact, conformal placement inside fluidic systems and integration with wireless potentiostat for convenient readout. Careful calibration examines how reaction kinetics and operating conditions such as the temperature and ionic strength of the sample affect measurement accuracy, consistency across sensors, and selectivity against non-phosphate anions.

To demonstrate relevance in practical applications, our sensors are used to detect phosphate levels in complex samples including artificial saliva and real-world wastewater influent. These two use-cases represent biomedical and environmental samples covering a broad range of ion concentrations. The results are validated through the standard

colorimetric molybdenum blue assay, confirming the accuracy of our sensors. This work bridges the well-established molybdate-phosphate recognition chemistry with device processing and operational insights to deliver a sensitive, portable, economical phosphate sensing platform for bioanalytical and environmental monitoring applications.

Results and discussion

We fabricated the sensor electrodes by stencil-printing conductive inks onto flexible polyethylene terephthalate (PET) substrates. The fabrication details are presented in the Materials and Methods section; in brief, the working electrode and counter electrode were patterned with a graphite ink, while the exposed surface of the reference electrode was printed with a Ag/AgCl ink as shown in **Figure 1a**.

A MoO_x film was electrodeposited onto the working electrode via cyclic voltammetry (CV) in an aqueous solution of 50 mM Na_2SO_4 and 5 mM $(NH_4)_6Mo_7O_{24}$ at a pH of 5. The deposition potential was selected to cycle between −0.6 V and 0.2 V versus Ag/AgCl to facilitate the partial reduction of Mo(VI) to Mo(V), forming a film of mixed-valence state[34] MoO_x where $x \leq 3$ with both Mo^{VI}/Mo^{V}, from the ammonium molybdate precursor. This mixed-valence state was confirmed by x-ray photoelectron spectroscopy on the Mo 3*d* peak in Supplemental Figure S1. The Raman spectrum of MoO_x in Supplemental Figure S2 further supports that the electrodeposited MoO_x is not a physical mixture of MoO_3 and MoO_2, but rather a disordered molybdenum oxide with mixed valence (Mo^{VI} and Mo^{V}). In **Figure 1b**, the cathodic current gradually decreased with more CV cycles, due to the growth of the MoO_x layer which limited further electron transfer at the electrode-electrolyte interface. The electrodeposition was carried out for 11 CV cycles, which consistently yielded a MoO_x film with a thickness of ~5 µm.

Following electrodeposition, the optical and scanning electron microscopy (SEM) images of the working electrode (**Figure 1c** and **1d**, respectively) revealed clear contrasts between the bare graphite surface and the region coated with MoO_x. Energy-dispersive x-ray spectroscopy (EDS) in Supplemental Figure S3 mapped the distribution of Mo and O across the electrode surface, confirming the elemental composition of the deposited film and its uniform coverage. After immersing the sensor electrode in an electrolyte with orthophosphate H_3PO_4 (hereafter shortened to phosphate), the electrode was washed in deionized water and dried for another round of EDS analysis, which detected the presence of phosphorus associated with the MoO_x-phosphate complex.

The electrodeposited MoO_x interacted with phosphate through coordination between Mo centers (Mo^{VI}/Mo^{V}) and H_3PO_4. This interaction led to the formation of redox-active MoO_x-phosphate complexes, which were most abundant in acidic conditions;[15,35] thus, subsequent measurements were conducted in aqueous electrolytes adjusted to a pH of 1 using ~0.1 M H_2SO_4. In **Figure 2a**, the square wave voltammetry (SWV) measurements display well-defined, reversible redox peaks in the presence of 100 µM phosphate (solid

blue line), compared to the featureless background current in the blank solution (dotted black line). The four redox peaks of MoO_x-phosphate complexes were centered around –0.18 V, 0.04 V, 0.17 V, and 0.32 V. It should be noted that the redox peak assignments for molybdate-based materials vary across different studies, as summarized in Supplemental Table S1. Due to the pH-dependent species and complex multiple electron transfer processes,[20,34] the detailed electrochemical mechanisms are still uncertain. But according to the XPS and Raman results, the peaks likely originated from oxidation of diverse Mo (V) centers in different redox environments associated with various crystallographic sites and ligands. Similar peak multiplicity has been observed in both polyoxomolybdates and amorphous MoO_x systems due to sequential electron transfer across non-equivalent Mo sites.[35,36] The symmetric peaks observed in forward and reverse scans confirmed the electrochemical stability even in harsh acidic environment, demonstrating that the mixed-valence MoO_x film provided robust phosphate recognition and reliable electrochemical signal transduction.

Characterizing sensitivity to phosphate under various operating conditions

Figure 2b shows a zoomed-in view of the forward SWV scan; in the following analyses, the sensor response was defined as the current difference (ΔI) between the redox peak at 0.17 V and the baseline level at 0.55 V. In comparing Figure 2a and 2b, where both scans were under the same 100 μM phosphate concentration, we noticed that the ΔI amplitudes were different due to the timing of the measurements, with the former recorded at 3 min and the latter at 13 min after adding the analyte solution onto the sensor. This observation pointed to the need for evaluating the sensor response as a function of time and temperature. As shown in **Figure 2c**, the ΔI responses initially increased with time and then reached a plateau around 10 minutes. Thus, upon sample exposure to the sensor, at least ten minutes was needed to establish equilibrium for the formation of MoO_x-phosphate complexes. Nonetheless, this waiting period was still much shorter than that of the standard molybdenum blue assay, which typically requires an hour.[16] The ΔI signals slightly increased at 37°C compared to room temperature, due to the enhanced kinetics with higher temperature. The kinetics measurements at 37 °C in Figure 2c were carried out to evaluate the sensor performance under physiological conditions, relevant for potential wearable or biomedical applications. All the measurements below were conducted at 25°C and recorded around 13 min after sample contact.

The sensor SWV redox current in **Figure 2d** increased with higher phosphate concentrations in the sample. Because of a small drift in baseline current level over time, as shown in Supplemental Figure S4, the SWV responses were baseline-corrected by subtraction, to align all curves to the baseline current at 0.55 V (I_{blank}) of the blank electrolyte without any phosphate (an aqueous solution of 0.1 M KCl and 0.1 M H_2SO_4). The corresponding calibration curve of ΔI versus phosphate analyte concentration in **Figure 2e** showed linearity over a wide dynamic range from 10 to 1000 μM. The linear response region was fitted to a logarithmic scale, resulting in the following best-fit values:

$$\Delta I \text{ in } \mu A = 5.1\ \mu A/\text{decade} \times \log_{10}[\text{phosphate concentration in } \mu M] - 3.9\ \mu A.$$

Thus the sensitivity slope was 5.1 μA/decade. Using the s-shaped calibration curve[37] and extrapolating from the intersection of the background Δ*I* level and the sensitivity slope, the detection limit was estimated to be 8 μM, equivalent to 800 parts per billion. Our MoO_x sensor shows a broader linear detection range compared to prior molybdate methods for phosphate detection listed in Supplemental Table S2. Earlier molybdate sensors were mostly made by drop-casting mixtures of ammonium heptamolybdate with different host materials. With this approach, while the initial sensitivity could be high, the molybdate was observed to redissolve during measurement, and the degree of dissolution would depend on the film thicknesses, drying conditions, and electrolyte compositions, which led to signal instability and poor reproducibility. While this work also used ammonium heptamolydate as a precursor, our improved performance is attributed to the electrodeposition that formed a MoO_x film more robust against dissolution than molybdate ions. Furthermore, previous works did not report on the effects of equilibration time on sensor signals and did not show stability over time. Future efforts on our MoO_x sensor may focus on optimizing the electrodeposition parameters for better sensitivity and detection limit.

To assess sensor stability, the device was tested by alternately exposing it to solutions with and without phosphate, as shown in **Figure 2f**. After the MoO_x electrode was exposed to 20 μM phosphate and then immersed in a blank electrolyte, the SWV responses were comparable (light blue solid and dotted lines, respectively), indicating that the MoO_x-phosphate complexes remained on the electrode and were not displaced by the blank electrolyte flow. With a second exposure to 20 μM phosphate followed by a blank electrolyte, the cumulative phosphate concentration on the sensor reached 40 μM, resulting in higher SWV peak currents (dark blue solid and dotted lines). The corresponding Δ*I* from these four scans are denoted by triangle symbols in Figure 2e and aligned with the calibration curve from another device. This consistency further confirmed the sensor-to-sensor reproducibility and measurement stability of single MoO_x sensor as Supplemental Figure S5, as well as the capability of MoO_x films to monitor cumulative phosphate exposure until the sensor reaches saturation. The strong retention of MoO_x-phosphate complexes on the electrode also suggests potential for phosphate recovery applications.[6–8]

Characterizing selectivity to phosphate over competing anions

The selectivity of the MoO_x sensor toward phosphate was assessed by examining possible interference by other anions commonly present in environmental and biological samples, including NO_3^-, CO_3^{2-}, and SiO_3^{2-}. At the measurement pH ~1, the anions may exist in various protonation states depending on their respective pKa values. For simplicity, below we denote the anion species by their basic anionic forms. **Figure 3a** compares the SWV responses before (black lines) and after the addition of 1 mM of sodium nitrate (red lines) to the sample solutions. The responses before and after NO_3^- addition were comparable. Even as the concentration of 1 mM NO_3^- was at a ten-fold excess relative to 100 μM phosphate in the sample, the MoO_x-phosphate redox peaks

were not interfered by the nitrate anions. Comparisons of SWV responses before and after adding 1 mM CO_3^{2-} and SiO_3^{2-} anions are shown in Supplemental Figure S6, showing negligible difference. These anions also did not interfere with phosphate detection, indicating that the redox signals were highly specific to the MoO_x-phosphate complex.

Figure 3b summarizes Δ*I* values for sample solutions without phosphate (left) and with 100 μM phosphate (right). The signal strength in the presence of additional 1 mM anions (color bars) was within measurement standard deviations of the original electrolyte (black/gray bars, with 0.1 M Cl^- and SO_4^{2-}). We note that among the tested anions, SiO_3^{2-} was an interference in conventional molybdenum blue assays because of its propensity to form heteropoly acids reducible to molybdenum blue species. However, in our MoO_x sensor, SiO_3^{2-} interference was effectively suppressed by sufficiently acidic conditions (pH ~1) and a short equilibration time (~13 min after sample exposure). In **Figure 3c**, the sensor calibration curves remained the same and unaffected by the additional anions, and the MoO_x sensor successfully distinguished phosphate in solutions containing background Cl^-, SO_4^{2-}, NO_3^-, CO_3^{2-}, and SiO_3^{2-} anions. The superior selectivity toward phosphate originated from its strong affinity to coordinate with molybdenum centers, enabling phosphate-specific redox response from MoO_x-phosphate complexes. The stable sensor performance in mixed-anion environment provided a strong basis for phosphate detection in complex samples.

Measuring phosphate levels in artificial saliva and real-world wastewater influent

To demonstrate their applicability in health diagnostics and environmental monitoring, the MoO_x sensors were used to determine phosphate concentrations in a sample of artificial human saliva purchased from Biochemazone (item# BZ323) and a field sample from a wastewater treatment plant located in St. Paul, Minnesota. These applications are relevant to public health, because abnormal phosphate levels in saliva[38,39] are a biomarker for kidney and oral diseases. The treatment of wastewater involves monitoring to remove excess phosphate.

As seen in **Figure 4a**, the flexible MoO_x sensor was integrated with a compact potentiostat (Zensor) with wireless data transmission. This configuration would be adaptable to microfluidic setups for measuring biofluids such as saliva or sweat, offering a path toward wearable health monitoring like on a mouthguard or a patch. **Figure 4b** shows the phosphate calibration curves of the sensor in two electrolytes with different ionic strengths: 0.1 M KCl (same data as in Figure 2e) and 1 M KCl. The 1 M KCl was included to simulate sample matrices with higher ionic strength such as urine and seawater. Compared to the 0.1 M KCl electrolyte, the use of 1 M KCl resulted in slightly lower signal intensity, likely due to stronger ionic shielding and a decrease in effective ion mobility with higher ionic strength. Nonetheless, since ionic strength correlates to conductivity measurable by printed electrodes,[40,41] the calibration curve can be adjusted accordingly to account for background variations.

Since typical phosphate concentrations in human saliva range between 0.8–2 mM, which is approaching the saturation limit of the sensor calibration curve, the artificial saliva sample was diluted to 1% by volume with a blank electrolyte, which was either the 0.1 M or 1 M KCl (both with 0.1 M H_2SO_4 for adjusting pH to 1). As shown in **Figure 4c**, the diluted sample was measured using three independently prepared MoO_x electrodes in each electrolyte. The redox peaks observed in 1 M KCl were shifted relative to those in the 0.1 M KCl electrolyte, and the Δ*I* values were extracted using the peak at 0.17 V for 0.1 M KCl, and the peak at 0.28 V for 1 M KCl. The Δ*I* values obtained from these measurements were marked by triangle symbols in the Figure 4b inset to determine the concentration of phosphate. The extrapolated concentrations from the inset were multiplied by a factor of 100 to account for the sample dilution. Thus, the phosphate levels in the artificial saliva sample were 1.59 ± 0.11 mM in 0.1 M KCl, and 1.73 ± 0.18 mM in 1 M KCl, closely matching the reported physiological value in healthy human saliva.

Phosphate detection was successfully achieved in complex biological matrices. Despite the difference in ionic strengths between 0.1 M and 1 M KCl backgrounds, the extracted phosphate concentrations were consistent when the appropriate calibration curve was applied. This consistency across different electrodes and electrolyte conditions underscored the sensor reliability and wide operational window, enabling convenient, point-of-use monitoring across diverse samples with varying ionic strengths.

For the field sample of wastewater influent, we determined its phosphate concentration using the standard addition method, which avoided the dilution of samples anticipated to have a low analyte concentration. The supporting electrolyte salts KCl and H_2SO_4 were directly added to the sample at 0.1 M each. As a concept illustrated in **Figure 4d**, the flexible MoO_x sensor could be placed inside a pipe for in-situ measurement during water treatment. **Figure 4e** shows the SWV responses of a representative electrode in the standard addition process. The sequence of measurements was first on the wastewater sample as collected (dashed brown line), which did not show redox response yet due to the lack of pH adjustment. After the sample was mixed with KCl and H_2SO_4 salts at 0.1 M each to achieve pH ~1, (i) the redox peaks were apparent (solid yellow line), indicating the presence of phosphate in the sample. The sensor response in a control electrolyte without phosphate served as the I_{blank} baseline (dotted black line). Following the measurement in step (i), successive additions of phosphate amounts (NaH_2PO_4 salts) were mixed into the sample, at a concentration of (ii) 50 μM (light blue line), then (iii) another 25 μM (medium blue line), and lastly (iv) another 25 μM (dark blue line). The Δ*I* of measurements (i)–(iv) were plotted in **Figure 4f** as a function of the total amount of added phosphate into the sample. The data were fitted to a linear trend line, and the x-intercept was obtained to infer the phosphate concentration in the sample. Using three independent sensors, the phosphate concentration of the wastewater influent was determined to be 68, 72, and 61 μM, yielding an average of 67 ± 5.7 μM of phosphate, corresponding to 2.1 ± 0.2 parts per million (ppm) of phosphorus. This value is in excellent agreement with the result of 2.3 ppm obtained using the conventional molybdenum blue

colorimetric assay as validation (Supplemental Figure S7), confirming the accuracy and reproducibility of the MoO_x electrochemical sensor for phosphate detection in complex environmental samples.

Conclusion

In this work, we developed a sensitive electrochemical sensor based on mixed-valence MoO_x for selective phosphate detection in complex aqueous environments. By integrating classic molybdate-phosphate coordination chemistry into a robust solid-state interface, the sensor enables electrochemical phosphate recognition with strong selectivity and operational robustness. The device exhibited linearity across a broad concentration range between 10 μM to 1 mM relevant to biological fluids and environmental samples and showed a phosphate detection limit of 8 μM. Direct detection was achieved in samples such as artificial saliva and wastewater influent, demonstrating tolerance to common background anions and varying ionic conditions. The prototype, combining stencil-printed electrodes and wireless signal acquisition, presents a promising route toward low-cost distributed sensing systems for phosphate.

Materials and methods

Sensor fabrication

For the fabrication of the stencil-printed electrodes,[40,41] 1 g of graphite powder (Alfa Aesar, particle size 1–2 μm) and 0.1 g of poly(vinylidene fluoride) (PVDF, Arkema Kynar HSV 900) were mixed in 2 mL of N-methyl-2-pyrrolidone (NMP, Sigma-Aldrich) and stirred overnight at room temperature to obtain a graphite-PVDF slurry. Then the slurry was deposited onto a flexible PET substrate (Immuson) via stencil printing to pattern the working electrode (WE) and counter electrode (CE). The WE diameter was 3 mm and the electrode design were shown in Supplemental Figure S8. The electrode stencil masks were cut using a digital blade-cutter (Silhouette Cameo). Ag/AgCl ink (Ercon, part#E2414) was deposited as the reference electrode (RE) using the same stencil printing technique. The printed electrodes were dried at 85 °C for 20 minutes on a hot plate in air. SWV measurements were conducted on screen-printed electrodes (Zensor SPE), which featured identical WE and CE geometries as the stencil-printed electrodes, ensuring that the electrochemical results obtained from both platforms were comparable with the same electrode surface area.

Electrodeposition of the mixed valence MoO_x film was carried out in an electrolyte containing 50 mM Na_2SO_4 and 5 mM $(NH_4)_6Mo_7O_{24}$ (pH~5) by applying cyclic voltammetry waveform via a potentiostat (BioLogic SP-200). The potential was scanned from –0.6 V to 0.2 V at a scan rate of 50 mV/s for 11 cycles. The electrode color became darker after MoO_x deposition.

Measurement methods

The MoO_x electrodes were rinsed with deionized water and air-dried at room temperature before morphological, compositional, and electrochemical characterization via SEM (FEI Apreo), XPS (Kratos AXIS-Supra), Raman (Renishaw inVia upright microscope) and SWV tests (BioLogic SP-200). Solutions with different phosphate concentrations were prepared by dissolving NaH_2PO_4 in aqueous electrolytes with 0.1 M H_2SO_4 and KCl either at 0.1 M or 1 M concentrations.

All SWV measurements were performed with a pulse height of 25 mV, a step height of 1 mV, and a pulse width of 10 ms, scanned from −0.27 V to 0.57 V in 0.1 M KCl or −0.14 V to 0.67 V in 1 M KCl. The error bars represent the standard deviations (SD) from 3 measurements and are drawn as ± SD of the data average. The SWV waveform is illustrated in Supplemental Figure S9. During each square wave cycle, the current was recorded at two times, one was at the end of the forward pulse (I_{fwd}) and another at the end of the reverse pulse (I_{rev}). The difference between these two measurements ($I_{fwd} - I_{rev}$) would yield the net current correlated to the analyte concentration. This differential approach suppressed background currents from capacitive contributions and enhanced detection sensitivity compared to steady-state techniques like CV or chronoamperometry.

Sample preparations

The artificial human saliva sample was used as received without any pretreatment. The wastewater influent samples were collected from a wastewater treatment plant in St. Paul, Minnesota in April 2024. After collection, the samples were stored at −20 °C, then thawed and filtered through a 0.22 μm nylon membrane prior to analysis.

Author contributions

S.Y. designed and conducted the experiments and analyzed the data. X.S. fabricated the stencil-printed electrodes. J.J. did SEM and XPS characterization. Z.Y. contributed to the design of kinetic experiments and sample validation by conventional molybdenum blue method. S.I. and C.T.H. collected environmental samples. S.I., C.T.H., V.C.P., A.H.F., J.D.A., and T.N.N. conceptualized and supervised the project. All authors contributed to discussions and writing of the manuscript.

Data availability

Supporting Information is available online.

Conflicts of interest

There are no conflicts of interest to declare.

Acknowledgements

The authors are grateful for the support from National Science Foundation (NSF) award OIA-2317825. The wireless electronics were purchased through the NSF award CNS-2408393.

References

(1) Duhamel, S.; Diaz, J. M.; Adams, J. C.; Djaoudi, K.; Steck, V.; Waggoner, E. M. Phosphorus as an Integral Component of Global Marine Biogeochemistry. *Nat Geosci* **2021**, *14* (6), 359–368. https://doi.org/10.1038/s41561-021-00755-8.

(2) Hargrove, A. E.; Nieto, S.; Zhang, T.; Sessler, J. L.; Anslyn, E. V. Artificial Receptors for the Recognition of Phosphorylated Molecules. *Chem Rev* **2011**, *111* (11), 6603–6782. https://doi.org/10.1021/cr100242s.

(3) Bhadada, S. K.; Ghosh, J.; Pal, R.; Mukherjee, S. Phosphate: An Underrated Component of Primary Hyperparathyroidism. *Best Pract Res Clin Endocrinol Metab* **2024**, *38* (2), 101837. https://doi.org/10.1016/j.beem.2023.101837.

(4) Brunelli, S. M.; Goldfarb, S. Hypophosphatemia: Clinical Consequences and Management. *Journal of the American Society of Nephrology* **2007**, *18* (7), 1999–2003. https://doi.org/10.1681/ASN.2007020143.

(5) Block, G. A.; Klassen, P. S.; Lazarus, J. M.; Ofsthun, N.; Lowrie, E. G.; Chertow, G. M. Mineral Metabolism, Mortality, and Morbidity in Maintenance Hemodialysis. *Journal of the American Society of Nephrology* **2004**, *15* (8), 2208–2218. https://doi.org/10.1097/01.ASN.0000133041.27682.A2.

(6) Jin, X.; Guo, J.; Hossain, M. F.; Lu, J.; Lu, Q.; Zhou, Y.; Zhou, Y. Recent Advances in the Removal and Recovery of Phosphorus from Aqueous Solution by Metal-Based Adsorbents: A Review. *Resour Conserv Recycl* **2024**, *204*, 107464. https://doi.org/10.1016/j.resconrec.2024.107464.

(7) Jupp, A. R.; Beijer, S.; Narain, G. C.; Schipper, W.; Slootweg, J. C. Phosphorus Recovery and Recycling-Closing the Loop. *Chem Soc Rev* **2021**, *50* (1), 87–101. https://doi.org/10.1039/d0cs01150a.

(8) Sarvajayakesavalu, S.; Lu, Y.; Withers, P. J. A.; Pavinato, P. S.; Pan, G.; Chareonsudjai, P. Phosphorus

Recovery: A Need for an Integrated Approach. *Ecosystem Health and Sustainability* **2018**, *4* (2), 48–57. https://doi.org/10.1080/20964129.2018.1460122.

(9) Correll, D. L. (1998) Role of Phosphorus in the Eutrophication of Receiving Waters: A Review, The. *J. Environ. Qual* **1998**, *27*, 261–266.

(10) Neal, J. F.; Zhao, W.; Grooms, A. J.; Smeltzer, M. A.; Shook, B. M.; Flood, A. H.; Allen, H. C. Interfacial Supramolecular Structures of Amphiphilic Receptors Drive Aqueous Phosphate Recognition. *J Am Chem Soc* **2019**, *141* (19), 7876–7886. https://doi.org/10.1021/jacs.9b02148.

(11) Cremer, P. S.; Flood, A. H.; Gibb, B. C.; Mobley, D. L. Collaborative Routes to Clarifying the Murky Waters of Aqueous Supramolecular Chemistry. *Nat Chem* **2017**, *10* (1), 8–16. https://doi.org/10.1038/NCHEM.2894.

(12) Dos Santos, C. M. G.; Fernández, P. B.; Plush, S. E.; Leonard, J. P.; Gunnlaugsson, T. Lanthanide Luminescent Anion Sensing: Evidence of Multiple Anion Recognition through Hydrogen Bonding and Metal Ion Coordination. *Chemical Communications* **2007**, No. 32, 3389–3391. https://doi.org/10.1039/b705560a.

(13) Huang, S. Y.; Qian, M.; Pierre, V. C. A Combination of Factors: Tuning the Affinity of Europium Receptors for Phosphate in Water. *Inorg Chem* **2019**, *58* (23), 16087–16099. https://doi.org/10.1021/acs.inorgchem.9b02650.

(14) Huang, S. Y.; Pierre, V. C. Achieving Selectivity for Phosphate over Pyrophosphate in Ethanol with Iron(III)-Based Fluorescent Probes. *JACS Au* **2022**, *2* (7), 1604–1609. https://doi.org/10.1021/jacsau.2c00200.

(15) Nagul, E. A.; McKelvie, I. D.; Worsfold, P.; Kolev, S. D. The Molybdenum Blue Reaction for the Determination of Orthophosphate Revisited: Opening the Black Box. *Anal Chim Acta* **2015**, *890*, 60–82. https://doi.org/10.1016/j.aca.2015.07.030.

(16) Chen, P. S.; Toribara, T. Y.; Warner, H. Microdetermination of Phosphorus. *Anal Chem* **1956**, *28* (11), 1756–1758.

(17) Dafner, E. V. Segmented Continuous-Flow Analyses of Nutrient in Seawater: Intralaboratory Comparison of Technicon AutoAnalyzer II and Bran+Luebbe Continuous Flow AutoAnalyzer III. *Limnol Oceanogr Methods* **2015**, *13* (10), 511–520. https://doi.org/10.1002/lom3.10035.

(18) Benasco, A. R.; Tropp, J.; Kaphle, V.; Chen, Y.; Zhao, W.; Eedugurala, N.; Ng, T. N.; Flood, A. H.;

Azoulay, J. D. Receptor Induced Doping of Conjugated Polymer Transistors: A Strategy for Selective and Ultrasensitive Phosphate Detection in Complex Aqueous Environments. *Adv Electron Mater* **2022**, *8* (7), 2101353. https://doi.org/10.1002/aelm.202101353.

(19) Altahan, M. F.; AbdelAzzem, M. A New Approach for Determination of Orthophosphate Based on Mixed Valent Molybdenum Oxide/Poly 1,2-Diaminoanthraquinone in Seawater. *Sci Rep* **2023**, *13* (1), 13634. https://doi.org/10.1038/s41598-023-40479-w.

(20) Lu, Y.; Lan, Q.; Zhang, C.; Liu, B.; Wang, X.; Xu, X.; Liang, X. Trace-Level Sensing of Phosphate for Natural Soils by a Nano-Screen-Printed Electrode. *Environ Sci Technol* **2021**, *55* (19), 13093–13102. https://doi.org/10.1021/acs.est.1c05363.

(21) Zhu, W.; Huang, X.; Zhang, Y.; Yin, Z.; Yang, Z.; Yang, W. Renewable Molybdate Complexes Encapsulated in Anion Exchange Resin for Selective and Durable Removal of Phosphate. *Chinese Chemical Letters* **2021**, *32* (11), 3382–3386. https://doi.org/10.1016/j.cclet.2021.04.027.

(22) Chen, C.; Wiorek, A.; Gomis-Berenguer, A.; Crespo, G. A.; Cuartero, M. Portable All-in-One Electrochemical Actuator-Sensor System for the Detection of Dissolved Inorganic Phosphorus in Seawater. *Anal Chem* **2023**, *95* (8), 4180–4189. https://doi.org/10.1021/acs.analchem.2c05307.

(23) Wei, H.; Luan, Y.; Pan, D. All-in-One Portable Microsystem for on-Site Electrochemical Determination of Phosphate in Turbid Coastal Waters. *Microchemical Journal* **2022**, *183*, 108079. https://doi.org/10.1016/j.microc.2022.108079.

(24) Arvas, M. B.; Gürsu, H.; Gençten, M.; Sahin, Y. Electrochemical Formation of Molybdenum Phosphate on a Pencil Graphite Electrode and Its Potential Application for the Detection of Phosphate Ions. *Analytical Methods* **2018**, *10* (35), 4282–4291. https://doi.org/10.1039/c8ay01653d.

(25) Kabir, M. F.; Rahman, M. T.; Gurung, A.; Qiao, Q. Electrochemical Phosphate Sensors Using Silver Nanowires Treated Screen Printed Electrodes. *IEEE Sens J* **2018**, *18* (9), 3480–3485. https://doi.org/10.1109/JSEN.2018.2808163.

(26) Wei, S.; Xiao, D.; Bian, C.; Li, Y. Phosphate and Nitrate Electrochemical Sensor Based on a Bifunctional Boron-Doped Diamond Electrode. *ACS Omega* **2024**, *9* (18), 20293–20303. https://doi.org/10.1021/acsomega.4c00717.

(27) Tang, C.; Fu, D.; Wang, R.; Zhang, X.; Wei, L.; Li, M.; Li, C.; Cao, Q.; Chen, X. An Electrochemical Microfluidic System for On-Site Continuous Monitoring of Soil Phosphate. *IEEE Sens J* **2024**, *24*

(5), 6754–6764. https://doi.org/10.1109/JSEN.2023.3348807.

(28) Pecunia, V.; Petti, L.; Andrews, J.; Ollearo, R.; Gelinck, G. H.; Nasrollahi, B.; Jailani, J. M.; Li, N.; Kim, J. H.; Ng, T. N.; Feng, H.; Chen, Z.; Guo, Y.; Shen, L.; Lhuillier, E.; Kuo, L.; Sangwan, V. K.; Hersam, M. C.; Fraboni, B.; Basirico, L.; Ciavatti, A.; Wu, H.; Niu, G.; Tang, J.; Yang, G.; Kim, D.; Dremann, D.; Jurchescu, O.; Bederak, D.; Shugla, A.; Costa, P.; Perinka, N.; Lanceros-Mendez, S.; Chortos, A.; Khuje, S.; Yu, J.; Ren, S.; Mascia, A.; Concas, M.; Cosseddu, P.; Young, R. J.; Yokota, T.; Somoya, T.; Jeon, S. J.; Zhaon, N.; Li, Y.; Shukla, D.; Wu, S.; Zhu, Y.; Takei, K.; Huang, Y.; Spiece, J.; Gehring, P.; Persaud, K.; Llobet, E.; Krik, S.; Vasquez, S.; Aurora Costa Angeli, M.; Lugli, P.; Fabbri, B.; Spagnoli, E.; Rossi, A.; Occhipinti, L. G.; Tang, C.; Yi, W.; Ravenscroft, D.; Kandukuri, T. R.; Ul Abideen, Z.; Azimi, Z.; Tricoli, A.; Rivadeneyra, A.; Rojas, S.; Gaiardo, A.; Valt, M.; Galstyan, V.; Zappa, D.; Comini, E.; Noel, V.; Mattana, G.; Piro, B.; Strand, E.; Bihar, E.; Whiting, G. L.; Shkodra, B.; Petrelli, M.; Moro, G.; Raucci, A.; Miglione, A.; Cinti, S.; Casson, A. J.; Wang, Z.; Bird, D.; Batchelor, J. C.; Xing, L.; Johnson, L. S. J.; Alwatter, A. A.; Kyndiah, A.; Viola, F. A.; Caironi, M.; Albarghouthi, F. M.; Smith, B. N.; Franklin, A. D.; Pal, A.; Banerjee, K.; Johnson, Z. T.; Claussen, J. C.; Moudgil, A.; Leong, W. L. Roadmap on Printable Electronic Materials for Next-Generation Sensors. *Nano Futures* **2024**, *8*, 032001. https://doi.org/10.1088/2399-1984/ad36ff.

(29) Ng, T. N.; Schwartz, D. E.; Mei, P.; Krusor, B.; Kor, S.; Veres, J.; Bröms, P.; Eriksson, T.; Wang, Y.; Hagel, O.; Karlsson, C. Printed Dose-Recording Tag Based on Organic Complementary Circuits and Ferroelectric Nonvolatile Memories. *Sci Rep* **2015**, *5* (August), 13457. https://doi.org/10.1038/srep13457.

(30) Wu, S.; Yao, L.; Shiller, A.; Barnard, A. H.; Azoulay, J. D. Dual-Gate Organic Electrochemical Transistors for Marine Sensing. *Adv Electron Mater* **2021**, *7*, 2100223. https://doi.org/10.1002/aelm.202100223.

(31) Ready, S.; Endicott, F.; Whiting, G.; Ng, T. N.; Chow, E.; Lu, J.-P. 3D Printed Electronics. *NIP & Digital Fabrication Conference* **2013**, *1*, 9–12.

(32) Kwon, K.; Ng, T. N. Improving Electroactive Polymer Actuator by Tuning Ionic Liquid Concentration. *Org Electron* **2014**, *15* (1), 294–298.

(33) Sulas, D. B.; London, A. E.; Huang, L.; Xu, L.; Wu, Z.; Ng, T. N.; Wong, B. M.; Schlenker, C. W.; Azoulay, J. D.; Sfeir, M. Y. Preferential Charge Generation at Aggregate Sites in Narrow Band Gap Infrared Photoresponsive Polymer Semiconductors. *Adv Opt Mater* **2018**, *6*, 1701138. https://doi.org/10.1002/adom.201701188.

(34) Shao, P.; Chang, Z.; Li, M.; Lu, X.; Jiang, W.; Zhang, K.; Luo, X.; Yang, L. Mixed-Valence Molybdenum Oxide as a Recyclable Sorbent for Silver Removal and Recovery from Wastewater. *Nat Commun* **2023**, *14* (1). https://doi.org/10.1038/s41467-023-37143-2.

(35) Tanaka, N.; Unoura, K.; Itabashi, E. Contribution from the Voltammetric and Spectroelectrochemical Studies of 12-Molybdophosphoric Acid in Aqueous and Water-Dioxane Solutions at a Gold-Minigrid Optically Transparent Thin-Layer Electrode. *Inorg. Chem* **1982**, *21*, 1662–1666.

(36) Laurans, M.; Mattera, M.; Salles, R.; K'Bidi, L.; Gouzerh, P.; Renaudineau, S.; Volatron, F.; Guillemot, G.; Blanchard, S.; Izzet, G.; Solé-Daura, A.; Poblet, J. M.; Proust, A. When Identification of the Reduction Sites in Mixed Molybdenum/Tungsten Keggin-Type Polyoxometalate Hybrids Turns Out Tricky. *Inorg Chem* **2022**, *61* (20), 7700–7709. https://doi.org/10.1021/acs.inorgchem.2c00866.

(37) Macchia, E.; Torricelli, F.; Bollella, P.; Sarcina, L.; Tricase, A.; Di Franco, C.; Österbacka, R.; Kovács-Vajna, Z. M.; Scamarcio, G.; Torsi, L. Large-Area Interfaces for Single-Molecule Label-Free Bioelectronic Detection. *Chem Rev* **2022**, *122* (4), 4636–4699. https://doi.org/10.1021/acs.chemrev.1c00290.

(38) Savica, V.; Calò, L.; Santoro, D.; Monardo, P.; Granata, A.; Bellinghieri, G. Salivary Phosphate Secretion in Chronic Kidney Disease. *Journal of Renal Nutrition* **2008**, *18* (1), 87–90. https://doi.org/10.1053/j.jrn.2007.10.018.

(39) Razzaque, M. S. Salivary Phosphate as a Biomarker for Human Diseases. *FASEB Bioadv* **2022**, *4* (2), 102–108. https://doi.org/10.1096/fba.2021-00104.

(40) Wu, S. E.; Shiller, A.; Barnard, A.; Azoulay, J. D.; Ng, T. N. Point-of-Use Printed Nitrate Sensor with Desalination Units. *Microchimica Acta* **2022**, *189* (6), 221. https://doi.org/10.1007/s00604-022-05314-5.

(41) Wu, S. E.; Phongphaew, N.; Zhai, Y.; Yao, L.; Hsu, H. H.; Shiller, A.; Azoulay, J. D.; Ng, T. N. Multiplexed Printed Sensors for in Situ Monitoring in Bivalve Aquaculture. *Nanoscale* **2022**, *359* (6371). https://doi.org/10.1039/d2nr04382c.

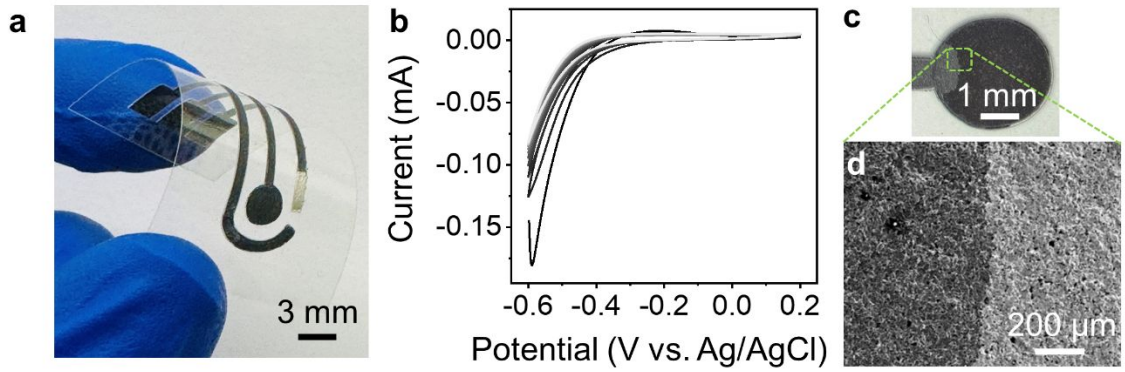

Fig. 1 Sensor design and fabrication. (a) Photograph of the sensor electrodes on a flexible plastic substrate. (b) Deposition cycles at a scan rate of 50 mV/s to form MoO_x from an aqueous solution of 5 mM $(NH_4)_6Mo_7O_{24}$ and 50 mM Na_2SO_4. The gray line indicates the final 11^{th} cycle. (c) Photograph and (d) scanning electron microscopy image of a MoO_x-coated electrode. The bare graphite surface was exposed on the left side and the MoO_x film on the right side.

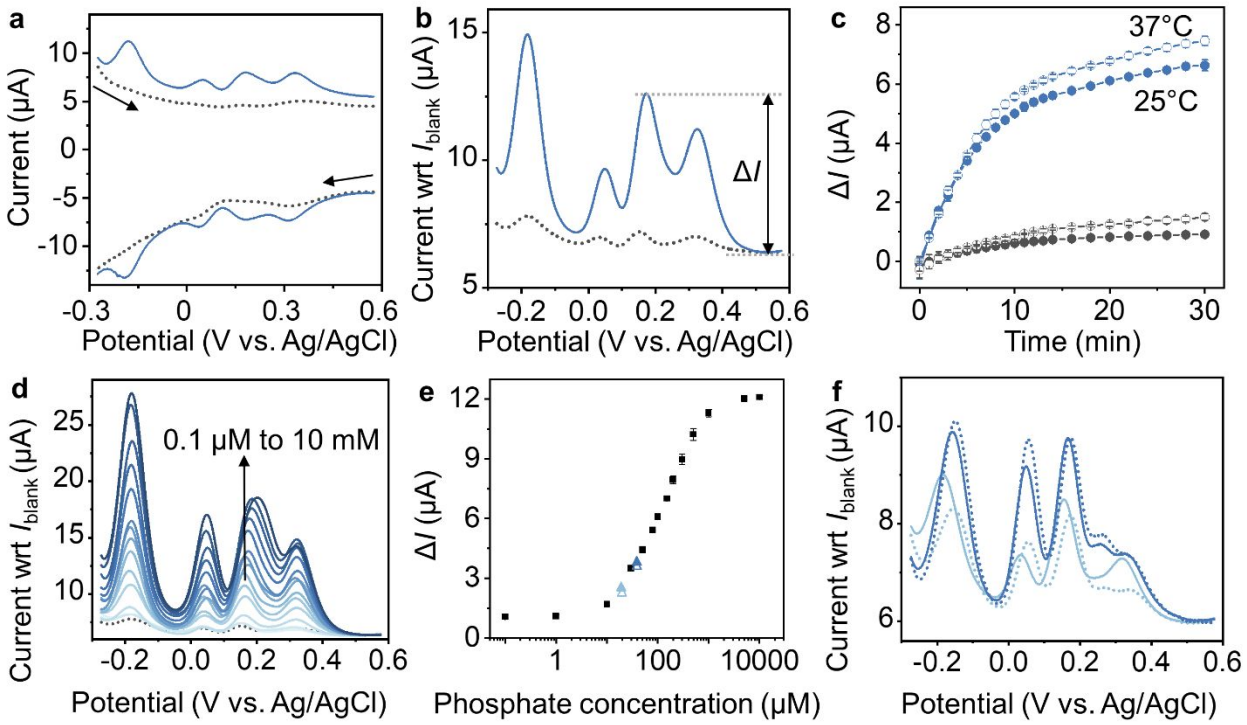

Fig. 2 Sensor response to phosphate. (a) Square wave voltammetry (SWV) of the MoO_x electrode in the absence (black dotted line) and presence (blue solid line) of 100 μM phosphate. Arrows indicate the direction of the voltage sweep. (b) Zoom-in view of the SWV responses under positive voltage sweep, with the current adjusted with respect to the baseline value at 0.55 V. (c) Current change versus time, at 25°C (solid circles) and 37°C (open circles), with (blue) and without (black) 100 μM phosphate. (d) SWV responses and (e) the calibration curve of the MoO_x electrode corresponding to phosphate concentrations ranging from 0.1 μM to 10 mM. (f) SWV responses across sequential scans: (1) first sample with 20 μM phosphate (light blue solid line); (2) then blank without phosphate (light blue dotted line); (3) second sample with 20 μM phosphate, leading to a cumulative exposure of 40 μM (dark blue solid line); and (4) blank again (dark blue dotted line). The corresponding Δ*I* from these four scans are denoted by triangle symbols in panel (e).

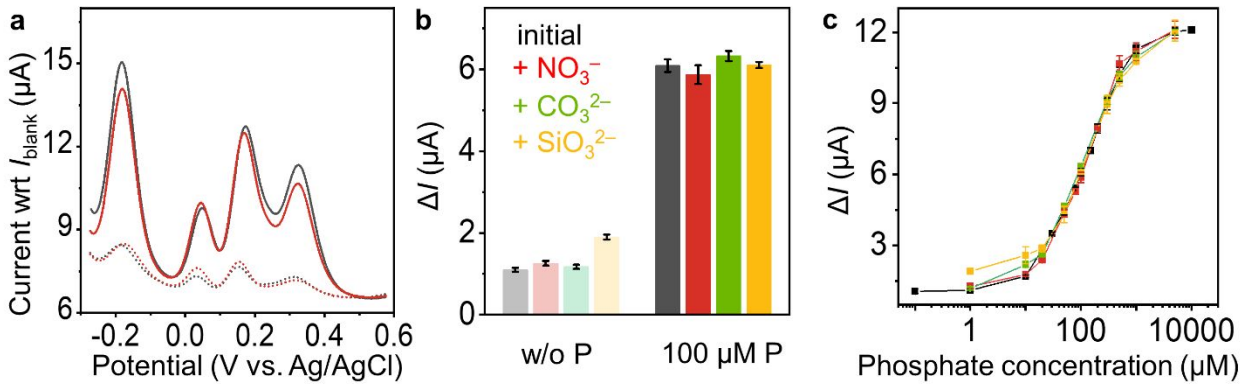

Fig. 3 Selectivity of the MoO_x sensor for phosphate compared to other anions. The same color legends apply to all panels. (a) SWV responses in the presence (solid lines) and absence (dotted lines) of 100 μM phosphate, without (black) and with (red) 1 mM $NaHNO_3$ in the sample electrolyte. (b) Δ*I* values for samples without or with 1 mM additional anions. (c) Calibration curves of the MoO_x electrode in an aqueous solution with 0.1 M KCl, 0.1 M H_2SO_4, and 1 mM anions as denoted by the color legend. The error bars represent the standard deviation (SD) from 3 measurements. Data are expressed as the mean ± SD.

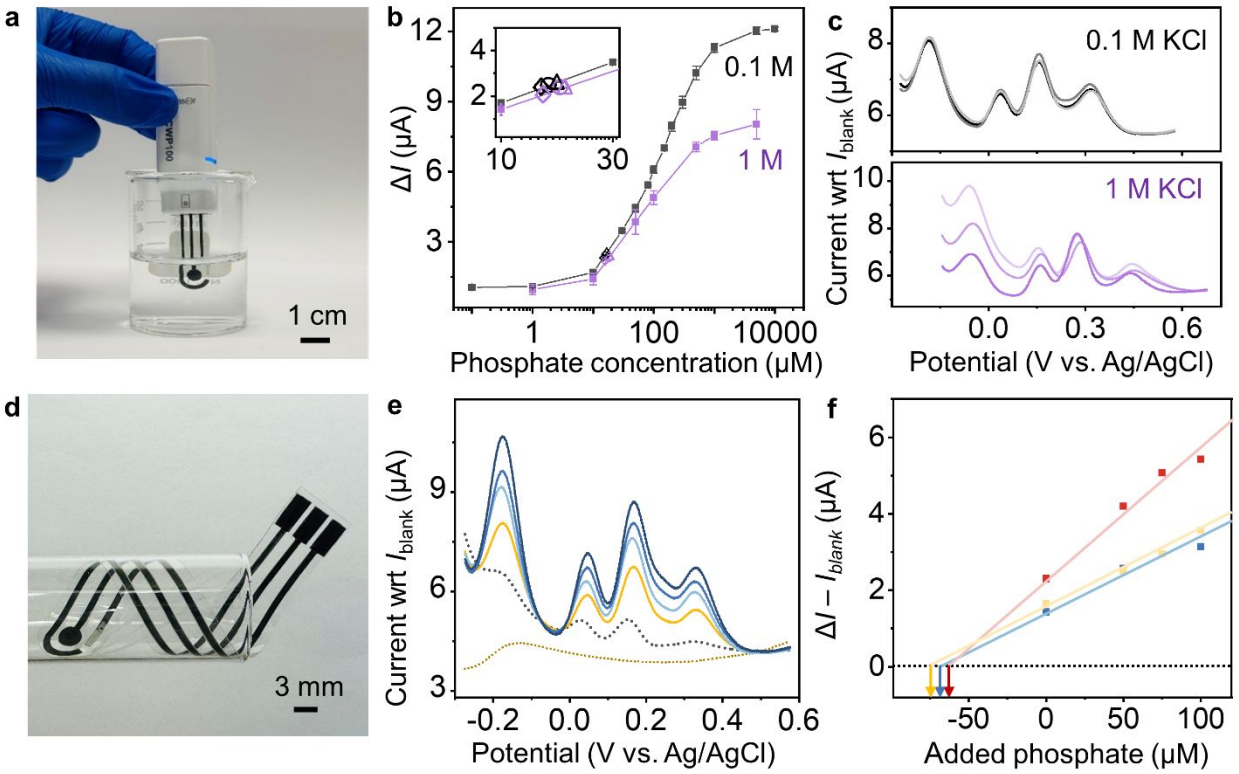

Fig. 4 Detection of phosphate in real-world samples. (a) Photograph of the point-of-use MoO_x sensor connected to a wireless potentiostat. (b) Calibration curves of the sensor in aqueous solutions with 0.1 M H_2SO_4 and 0.1 M (black) or 1 M KCl (purple). The inset zooms in on the samples measured in panel (c). (c) SWV responses for phosphate detection in artificial saliva samples. The same sample was diluted to 1% by volume in electrolytes of varying ionic strengths and measured using three individual sensors to demonstrate reproducibility. (d) Photograph of the flexible sensor, allowing easy integration inside a pipe or in fluidic systems. (e) SWV responses for an influent wastewater sample measured via the standard addition method. The sequence of measurements was the wastewater sample as collected (dashed brown line), (1) the sample mixed with KCl and H_2SO_4 salts at 0.1 M each (solid yellow line), followed by successive additions of phosphate into the mixture (2) at 50 μM (light blue line), then (3) another 25 μM (medium blue line), and lastly (4) another 25 μM PO_4^{3-} (dark blue line). The sensor response in the aqueous electrolyte without phosphate (black dotted line, 0.1 M KCl and 0.1 M H_2SO_4) served as the I_{blank} baseline. (f) The corresponding calibration curves derived from (e), repeated using three individual sensors on the same sample.